

# PHOTONICS Research

## Si-substrate vertical-structure InGaN/GaN micro-LED-based photodetector for beyond 10 Gbps visible light communication

JIANYANG SHI,<sup>1,2,3</sup>  ZENGYI XU,<sup>1</sup> WENQING NIU,<sup>1</sup> DONG LI,<sup>1</sup> XIAOMING WU,<sup>4</sup> ZIWEI LI,<sup>1,2,3,5</sup>   
JUNWEN ZHANG,<sup>1,2,3,5</sup>  CHAO SHEN,<sup>1,2,3,5,6</sup>  GUANGXU WANG,<sup>4</sup> XIAOLAN WANG,<sup>4</sup> JIANLI ZHANG,<sup>4,7</sup>  
FENGYI JIANG,<sup>4</sup> SHAOHUA YU,<sup>5</sup> AND NAN CHI,<sup>1,2,3,8</sup> 

<sup>1</sup>Key Laboratory for Information Science of Electromagnetic Waves (MoE), Fudan University, Shanghai 200433, China

<sup>2</sup>Shanghai Engineering Research Center of Low-Earth-Orbit Satellite Communication and Applications, Shanghai 200433, China

<sup>3</sup>Shanghai Collaborative Innovation Center of Low-Earth-Orbit Satellite Communication Technology, Shanghai 200433, China

<sup>4</sup>National Institute of LED on Silicon Substrate, Nanchang University, Nanchang 330096, China

<sup>5</sup>Peng Cheng Laboratory, Shenzhen 518055, China

<sup>6</sup>e-mail: chaoshen@fudan.edu.cn

<sup>7</sup>e-mail: zhangjianli@ncu.edu.cn

<sup>8</sup>e-mail: nanchi@fudan.edu.cn

Received 30 May 2022; revised 2 August 2022; accepted 9 August 2022; posted 16 August 2022 (Doc. ID 465455); published 30 September 2022

Visible light communication (VLC) has emerged as a promising communication method in 6G. However, the development of receiving devices is much slower than that of transmitting devices, limited by materials, structures, and fabrication. In this paper, we propose and fabricate an InGaN/GaN multiple-quantum-well-based vertical-structure micro-LED-based photodetector ( $\mu$ PD) on a Si substrate. A comprehensive comparison of the photoelectrical performance and communication performance of three sizes of  $\mu$ PDs, 10, 50, and 100  $\mu$ m, is presented. The peak responsivity of all three  $\mu$ PDs is achieved at 400 nm, while the passband full-widths at half maxima are 87, 72, and 78 nm for 10, 50, and 100  $\mu$ m  $\mu$ PDs, respectively. The -20 dB cutoff bandwidth is up to 822 MHz for 50  $\mu$ m  $\mu$ PD. A data rate of 10.14 Gbps is experimentally demonstrated by bit and power loading discrete multi-tone modulation and the proposed digital pre-equalizer algorithm over 1 m free space utilizing the self-designed  $4 \times 4$  50  $\mu$ m  $\mu$ PD array as a receiver and a 450 nm laser diode as a transmitter. This is the first time a more than 10 Gbps VLC system has been achieved utilizing a GaN-based micro-PD, to the best of our knowledge. The investigation fully demonstrates the superiority of Si substrates and vertical structures in InGaN/GaN  $\mu$ PDs and shows its great potential for high-speed VLC links beyond 10 Gbps. © 2022 Chinese Laser Press

<https://doi.org/10.1364/PRJ.465455>

### 1. INTRODUCTION

Next-generation communication (6G) has brought new challenges to transmission rates in recent years, and new spectrum resources, such as visible light, millimeter wave, and terahertz wave, have become a prominent research area [1–5]. Among these spectrum resources, visible light communication (VLC) offers a cheaper deployment cost than others since it permits both illumination and communication. Compared to traditional wireless communications, VLC operates in the 400–800 THz range, and has different physical features, such as great electromagnetic interference resistance, high confidentiality, and high data rate. Based on these, VLC is projected to become a powerful air interface technology in 6G [4].

Nonetheless, signal communication at such a short wavelength (about 400–780 nm) presents significant hurdles to

both transmitting and receiving devices. During the last decade, data rate breakthroughs in VLCs have focused mainly on transmitter devices, including light-emitting diodes (LEDs) [6–8], superluminescent diodes (SLDs) [9–11], and laser diodes (LDs) [12,13]. Using off-the-shelf LEDs and wavelength division multiplexing (WDM) technology, transmission rates of 15.73 Gbps have been achieved over a 1.6 m wireless link [6]. GaN-based micro-LEDs with reduced active areas offer large bandwidth and high power potential and have demonstrated the ability to transmit 10.11 Gbps over 5 m [7]. In addition to the aforementioned sapphire substrate LEDs, silicon (Si) substrate LEDs also have good performance. Based on Si-LED and 8- $\lambda$  WDM technology, the transmission rate can reach 24.25 Gbps [8]. With the advantages of high power, high brightness, and low coherence, the GaN-based SLD has been

verified to be able to transmit 4.57 Gbps [9]. An LD has a much higher bandwidth, and can be combined with 3- $\lambda$  WDM technology to achieve 46.4 Gbps transmission [12]. However, the vast majority of the above work is based on Si-based commercial photodetectors (PDs) or GaAs-based PDs.

In the infrared wavelength range, InGaAs-based PDs are already capable of supporting 100 Gbps optical communications [14]. The peak response of GaAs-based PDs is closer to visible light, but the bandwidth gradually decreases and remains in the near-infrared (NIR) region (e.g., Newport 818-BB-45A, 500–890 nm, peak at 830 nm). If the peak response is needed to move farther towards visible light, then the PD material requires the use of Si. The peak response of this type of PD is still near the NIR spectrum, and the wavelength response is particularly wide (e.g., MenloSystems APD210, 400–1000 nm, peak at 800 nm). Underwater optical communication based on blue or green lasers has been demonstrated to be feasible by utilizing the wide wavelength response of Si-based PDs [15,16]. However, the gap between the response at blue or green wavelength and the peak response is still large, which means that there is still a lot of signal-to-noise ratio (SNR) gain that can be improved for VLC. Furthermore, Si-based PDs are easily fabricated but are similarly less robust to harsh environments, such as space or seawater [17]. Considering this, a III-nitride-based PD is proposed to sense short wavelength signals, such as visible light and ultraviolet (UV). PDs based on GaN, AlGaIn, or InGaIn materials are built mainly on metal–semiconductor–metal (MSM) structures [18–20], p–i–n structures [20–22], and multiple quantum-well (MQW) structures [23–25]. A variety of optical wireless transmissions using MQW p–i–n-based PDs have recently been reported [17,26–31]. A record-breaking 3.2 Gbps transmission rate is achieved over 0.5 m fiber and 0.1 m free space utilizing an InGaIn/GaN MQW micro-PD ( $\mu$ PD) and 16-quadrature amplitude modulation (16-QAM) with orthogonal frequency-division multiplexing (OFDM) [17]. Employing an InGaIn/GaN MQW  $\mu$ PD array and on–off keying (OOK) modulation, a 350 Mbps multiple-input multiple-output system is demonstrated [26]. A semipolar InGaIn/GaN MQW  $\mu$ PD grown on a semipolar GaN substrate is proposed, and an OOK signal of 1.55 Gbps can be transmitted over 1 m using this  $\mu$ PD [27]. Further, the same group has implemented a semipolar InGaIn/GaN MQW  $\mu$ PD combined with bit and power loading OFDM to achieve a remarkable 7.4 Gbps rate in the violet range [28]. A 60 Mbps underwater wireless optical communication (UWOC) system was experimentally demonstrated with an InGaIn  $\mu$ PD array over a 2.3 m long water tank [29]. Recently, based on a semipolar InGaIn/GaN MQW  $\mu$ PD array, a research team was able to achieve 300 Mbps over 1.25 m [30] and 540 Mbps over 1.1 m [31] with OOK. Considering the relationship between transmission distance and data rate, we summarize the benchmark of the distance-rate product versus reverse bias voltage for a GaN-based  $\mu$ PD, as shown in Fig. 1. Neither the transmission rate nor the distance-rate product can fulfill the demand for 10 Gbps high-speed optical wireless communication [32].

However, almost all reported GaN-based  $\mu$ PDs are grown on sapphire substrates or GaN substrates. Due to the

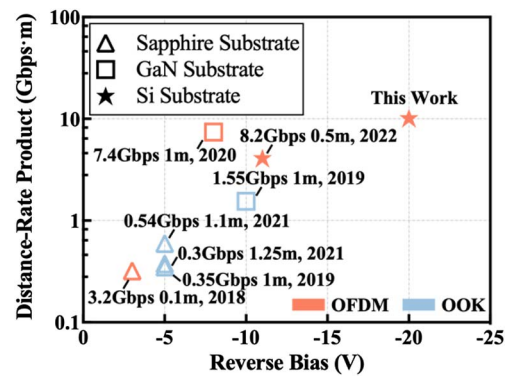


**Fig. 1.** Benchmark of distance-rate product versus reverse bias voltage for micro-LED-based photodetectors.

non-conductivity and low thermal conductivity of sapphire substrates, sapphire-based LEDs and  $\mu$ PDs are often fabricated in lateral structures, which can bring current crowding and current droop under a high injection current density or high incident light power. A GaN substrate is the most ideal substrate for growing GaN-based LEDs and  $\mu$ PDs, but it faces problems such as difficulty in production and high price for commercial use. Si substrates are another promising option to grow GaN-based LEDs or  $\mu$ PDs due to the advantages of low cost, large size, high crystal quality, better conductivity, and great thermal conductivity [33]. In recent years, InGaIn/GaN MQW LEDs fabricated on Si (111) (Si-substrate LED) have shown impressive results as transmitting devices in high-speed VLC systems [8,34]. Nevertheless, as a receiving device, a Si-substrate MSM UV PD is proposed, but the transmission performance in VLC links has yet to be experimentally investigated [35]. Our previous work has experimentally demonstrated for the first time the possibility of Si-substrate LEDs as PDs [36].

In this paper, an InGaIn/GaN MQW-based vertical-structure micro-LED-based PD on a Si substrate is proposed and fabricated. The photoelectrical performances of three different sizes of our designed  $\mu$ PDs are investigated, including 10, 50, and 100  $\mu$ m. The peak responsivity of all three  $\mu$ PDs is achieved at 400 nm, while the passband full-widths at half maximum (FWHMs) are 87 nm (375–462 nm), 72 nm (382–454 nm), and 78 nm (382–460 nm) for 10, 50, and 100  $\mu$ m  $\mu$ PDs, respectively. Such large FWHMs provide the feasibility of  $\mu$ PDs as a receiver in WDM VLC systems. Utilizing the self-designed  $4 \times 4$  50  $\mu$ m  $\mu$ PD array, a 10.14 Gbps 1 m VLC link is experimentally demonstrated by bit and power loading discrete multitone (DMT) modulation and the proposed digital pre-equalizer algorithm under the hard decision-forward error correction (HD-FEC) threshold of  $3.8 \times 10^{-3}$ . When the transmission distance is reduced to 0.5 m, the transmission rate can reach 7.58 Gbps for a 10  $\mu$ m  $\mu$ PD array, 10.81 Gbps for 50  $\mu$ m, and 7.18 Gbps for 100  $\mu$ m. To the best of our knowledge, this is the first time a transmission rate of more than 10 Gbps has been achieved utilizing a GaN-based PD. These results demonstrate the superiority of Si substrates and vertical structures in InGaIn/GaN  $\mu$ PDs and show their great potential for high-speed VLC links beyond 10 Gbps.

## 2. FABRICATION AND CHARACTERIZATION

### A. Design and Fabrication of Si-Substrate Micro-LED-Based Photodetector

In this experiment, we fabricate vertical GaN-based micro-LEDs on Si substrates. Considering the triangular symmetry relationship between the Si (111) and GaN (0001) planes, the Si (111) substrate is the best choice for the growth of *c*-plane GaN [37]. The proposed micro-LED samples are grown on a patterned Si (111) substrate by a self-developed metalorganic chemical vapor deposition (MOCVD) reactor. Trimethylaluminum (TMAl), trimethylgallium (TMGa), trimethylindium (TMIn), and ammonia (NH<sub>3</sub>) are used as source materials during growth for Al, Ga, In, and N, respectively. To overcome the lattice mismatch (17%,  $a_{\text{GaN}} = 0.3189$  nm,  $a_{\text{Si}} = 0.3840$  nm) and thermal mismatch (46%,  $5.59 \times 10^{-6}$  K<sup>-1</sup> for GaN,  $2.59 \times 10^{-6}$  K<sup>-1</sup> for Si) between the Si substrate and GaN, a 110 nm AlN ( $a_{\text{AlN}} = 0.3112$  nm) buffer layer is used on top of the Si substrate [38]. Subsequently, a silane (SiH<sub>4</sub>)-based Si-doped N-type GaN layer is deposited and followed by a low-temperature GaN (LT-GaN) layer, a superlattice (SL) interlayer (32 periods of In<sub>0.1</sub>Ga<sub>0.9</sub>N/GaN, 5/2 nm), and eight periods of In<sub>0.3</sub>Ga<sub>0.7</sub>N/GaN (2.5/13.5 nm) multiple quantum wells (MQWs). V-pit defects are introduced on the surface of the MQW layers, enhancing the In component and improving crystal quality. V-pit enables the active region to transition from a conventional planar structure to a three-dimensional one by introducing a horizontal p-n junction in addition to the initial vertical p-n junction. Coordination of the two directions of the p-n junction can control the carrier transport paths as well as the combination position, thus improving the LED performance, including emission and light detection [39,40]. Finally, a p-Al<sub>0.2</sub>Ga<sub>0.8</sub>N electron blocking layer (EBL) and a bis(cyclopentadienyl) magnesium (Cp2Mg)-based Mg-doped P-type GaN layer is grown on the top.

After epitaxial growth, the epitaxial wafer is fabricated into 10  $\mu\text{m} \times 10 \mu\text{m}$ , 50  $\mu\text{m} \times 50 \mu\text{m}$ , and 100  $\mu\text{m} \times 100 \mu\text{m}$  vertical structured micro-LED chips. First, a layer of metallic Ag with high reflectivity, which has good ohmic contact with P-GaN, is formed on the Ni-assisted-annealed epitaxial wafer using an electron beam evaporator [41]. This Ag reflector can improve not only the efficiency of single-side luminescence as transmitting, but also the efficiency of single-side detection as receiving. In addition to this, high impedance complementary electrodes (CEs, SiO<sub>2</sub>, or Si<sub>3</sub>N<sub>4</sub>) are deposited between the Ag reflector layer and the P-GaN to limit the area below the N-electrode and the passivation layer so that no current can pass through it. CE can significantly improve the light extraction efficiency of LED chips by alleviating current crowding [38,42]. Next, the wafer is bonded to the heat-conducting Si submount through the middle bonding layer. Another side of the Si submount is a metal protection layer. Then, we remove the Si substrate and AlN buffer layer using a wet etching process based on a mixed solution of HF, HNO<sub>3</sub>, and CH<sub>3</sub>COOH, and invert the remaining film such that the N-GaN layer is up. The n-GaN surface is then roughened, by immersing it in an 85°C and 20% mass concentration KOH solution. Before placing the N-electrode, the SiO<sub>2</sub>

surface passivation layer needs to be grown on the sidewall because the inductively coupled plasma (ICP) etching in the micro-LED chip manufacturing process will cause etching damage near the chip sidewalls. As the LED chip size gradually decreases, the ratio of sidewalls to the total area of the chip gradually increases, and the proportion of defects formed by etching damage gradually increases. These defects lead to a gradual increase in the proportion of non-radiative recombination, reducing luminous efficiency, but also the introduction of new leakage channels to increase the reverse leakage current. The schematic of the vertical structure of the Si-substrate micro-LED is shown in Fig. 2(a). Single-side luminescence based on a vertical structure can greatly improve the luminescence efficiency [38], so it is also expected to greatly improve the efficiency of light reception. The scanning electron microscope (SEM) images of 10  $\mu\text{m} \times 10 \mu\text{m}$ , 50  $\mu\text{m} \times 50 \mu\text{m}$ , and 100  $\mu\text{m} \times 100 \mu\text{m}$  micro-LED chips are shown in Figs. 2(b)–2(d). The white dots on the chip in the figure are the roughening surfaces of GaN. In the following sections, the three different sizes of chips will be called 10, 50, and 100  $\mu\text{m}$  micro-LEDs or  $\mu\text{PDs}$  for short.

On the basis of the above micro-LED chips, 4 × 4 LED arrays are manufactured as shown in Fig. 3(a). The center point pitch of the micro-LED chips is 300  $\mu\text{m}$ . The array is designed with a common cathode and the output of the cathode is placed in the center to achieve parallel connection of chips. This achieves the shortest global current transmission distance and symmetry. Figures 3(b), 3(c), and 3(d) show the optical microscope images of 10, 50, and 100  $\mu\text{m}$  micro-LED arrays, respectively. In the final step, the micro-LED array chips are connected directly to the heat sink of the holder through the conductive silver paste. Then, we assemble the lens on the LED package holder and inject high-transmittance, high-refractive-index epoxy silicone resin (Dow Corning OE-6662, refractive index 1.53, transmittance 90%) in the gap between the lens and the LED package module. Finally, the packaged micro-LED is heated in a 150°C oven for 1 h while the silicone cures.

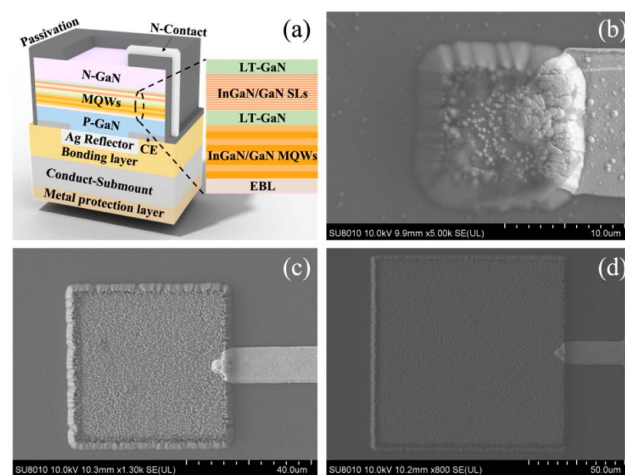


**Fig. 2.** (a) Schematic of the vertical structure of Si-substrate micro-LED-based photodetector; SEM images of (b) 10  $\mu\text{m}$ , (c) 50  $\mu\text{m}$ , and (d) 100  $\mu\text{m}$  chips.



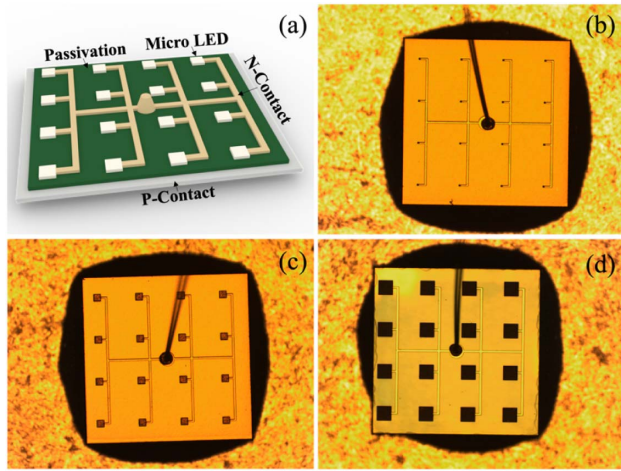


**Fig. 3.** (a) Schematic of layout for  $4 \times 4$  Si-substrate micro-LED array; optical microscope images of (b) 10  $\mu\text{m}$ , (c) 50  $\mu\text{m}$ , and (d) 100  $\mu\text{m}$  micro-LED array.

### B. Optical and Electrical Characteristics

We begin by evaluating the optical and electrical characteristics of three micro-LEDs. Figures 4(a), 4(b), and 4(c) show the responsivity spectra of 10, 50, and 100  $\mu\text{m}$  micro-LED-based PDs under different reverse bias voltages, respectively. The micro-LED chips are illuminated by monochromatic light from a 250 W xenon lamp (350–700 nm) passing through a monochromator (Newport CS260-USB-2-MT-D). The peak responsivity of all three  $\mu\text{PDs}$  is achieved at 400 nm. As the reverse bias voltage increases, the wavelength selectivity does not drift, but only increases the response intensity. The FWHMs are 87 nm (375–462 nm), 72 nm (382–454 nm), and 78 nm (382–460 nm) for 10, 50, and 100  $\mu\text{PDs}$ , respectively. Such large wavelength selection ranges greatly

increase the feasibility of  $\mu\text{PDs}$  as visible light receivers for WDM systems.

The emission spectra of micro-LEDs are also measured by a high-sensitivity spectrometer (Ocean Insight QE Pro-ABS) under various driven currents, as shown in Figs. 4(d)–4(f). The emission peak appears blueshifted as the injected current increases, which is due to the band filling effect [43]. At low current density, the emission peak wavelengths are 626, 596, and 600 nm for 10, 50, and 100  $\mu\text{m}$  micro-LEDs, respectively. At high current density, they can be 582, 573, and 577 nm, respectively. The difference between the peak response wavelength and peak emission wavelength is due to the different locations of light absorption and light emission.

Figures 5(a) and 5(b) show the current–voltage curve under the dark condition at reverse bias and forward bias voltages. Three  $\mu\text{PDs}$  exhibit dark currents of  $1.1 \times 10^{-6}$  A,  $3.5 \times 10^{-8}$  A, and  $8.0 \times 10^{-8}$  A at  $-20$  V, and the corresponding dark current densities are 1.1, 0.0014, and 0.0008 A/cm<sup>2</sup>, respectively. In addition, the turn-on voltage of all three micro-LEDs is relatively low, probably around 1.74 V. Figure 5(c) shows the photocurrent under 450 nm illumination at  $-20$  V before the electrical amplifier (EA). As the incident light power increases, the photocurrent continues to rise. There is a clear separation between dark currents and photocurrents by up to four orders of magnitude for 50 and 100  $\mu\text{m}$ , while it is only three for 10  $\mu\text{m}$ . This can provide a sufficiently high SNR for high-speed communications. Further, considering that the resistance–capacitance (RC) delay affects the bandwidth, we measured the capacitance at different reverse bias voltages by a semiconductor parameter analyzer (Keysight B1500A) as shown in Table 1. According to the measurement results, the capacitance of 10  $\mu\text{PD}$  is 42.1 pF at  $-10$  V, which corresponds to an RC-delay bandwidth of 75.6 MHz [17], while it is (59.8, 53.2) for 50  $\mu\text{m}$  and (108, 29.5) for 100  $\mu\text{m}$ . The load resistance is 50  $\Omega$  for all  $\mu\text{PDs}$ .

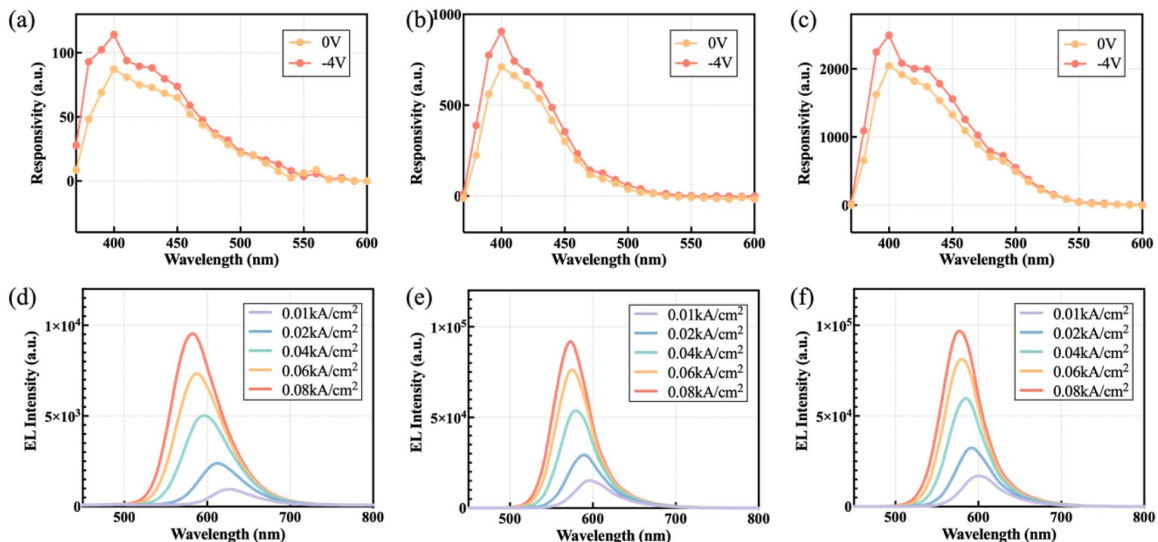


**Fig. 4.** Responsivity spectra of (a) 10  $\mu\text{m}$ , (b) 50  $\mu\text{m}$ , and (c) 100  $\mu\text{m}$  micro-LED-based photodetectors; electroluminescence spectra of (d) 10  $\mu\text{m}$ , (e) 50  $\mu\text{m}$ , and (f) 100  $\mu\text{m}$  micro-LEDs.

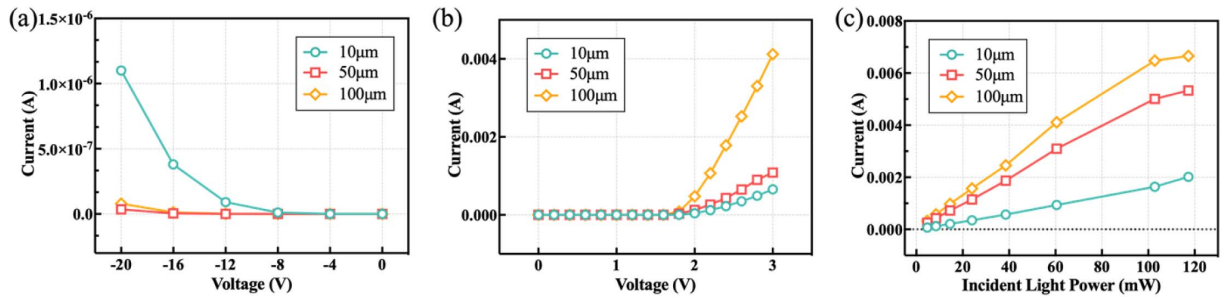


**Fig. 5.** Current–voltage ( $I$ - $V$ ) characteristics under the dark condition at (a) reverse bias and (b) forward bias; (c) photocurrent versus incident light power under the illumination of 450 nm light at  $-20$  V.

**Table 1. Capacitance versus Voltage of Micro-LED-Based Photodetectors**

Bias	Capacitance		
	10 $\mu\text{m}$	50 $\mu\text{m}$	100 $\mu\text{m}$
0 V	43.8 pF	92.6 pF	196.6 pF
-4 V	42.5 pF	68.7 pF	137.4 pF
-8 V	42.2 pF	61.0 pF	111.5 pF
-10 V	42.1 pF	59.8 pF	108.0 pF

### 3. PRINCIPLE AND EXPERIMENTAL SETUP

#### A. Principle of Operation

DMT modulation is a straightforward way to achieve real-value OFDM modulation, especially for VLC [8,34]. The advantage of multi-carrier modulation is that bit and power loading can be applied. The Levin–Campello (LC) algorithm is a classical bit and power joint optimization method that achieves maximum transmission rate at a certain power [44,45]. Another approach to improve the spectral efficiencies (SEs) of VLC is to use a pre-equalization circuit. Experiments have demonstrated that the modulation bandwidth can be increased from several tens of megahertz to 400–500 MHz using a suitable circuit, such as a T-bridge passive resonant circuit [46–48]. However, such a T-bridge structure circuit is limited by the device bandwidth, which can pose a hardware challenge when the modulation bandwidth is increased. Another challenge is that the analog domain hardware pre-equalization circuit does not facilitate

adaptive changes. Therefore, considering that hardware equalization is changing the frequency domain response, the linear digital domain pre-equalizer method is proposed to emulate the hardware pre-equalization circuit. A better data rate performance with the digital pre-equalizer is experimentally demonstrated.

The digital signal processing (DSP) implemented in this experiment is shown in Fig. 6. The whole transmission process is divided into an SNR estimation phase and a bit power loading phase. A quadratic phase-shift keying (QPSK) signal is used to estimate the SNR at every subcarrier. The total number of subcarriers is 1024, containing the signal (512 subcarriers) and its conjugate symmetry to form Hermitian symmetry. Zero padding subcarriers are also utilized in the low-frequency portion of the signal to avoid the influence of devices similar to a bias tee, and the number is eight. Before inverse fast Fourier transform (IFFT), the signal is unsampled by a factor of two. The generated DMT signal  $x(t)$  before the digital pre-equalizer can be denoted as

$$x(t) = \sum_{k=0}^{N_f-1} P(k)X(k)e^{j\frac{2\pi}{N_f}kt}, \quad (1)$$

where  $N_f$  is the product of the total number of subcarriers and the upsampling factor  $u$ .  $P(k)$  is the value after power allocation, and it will be equal to one at the SNR estimation phase.  $X(k)$  is the data on the  $k$ th subcarrier.

Then the signal is processed in a digital pre-equalizer process with the following expression:

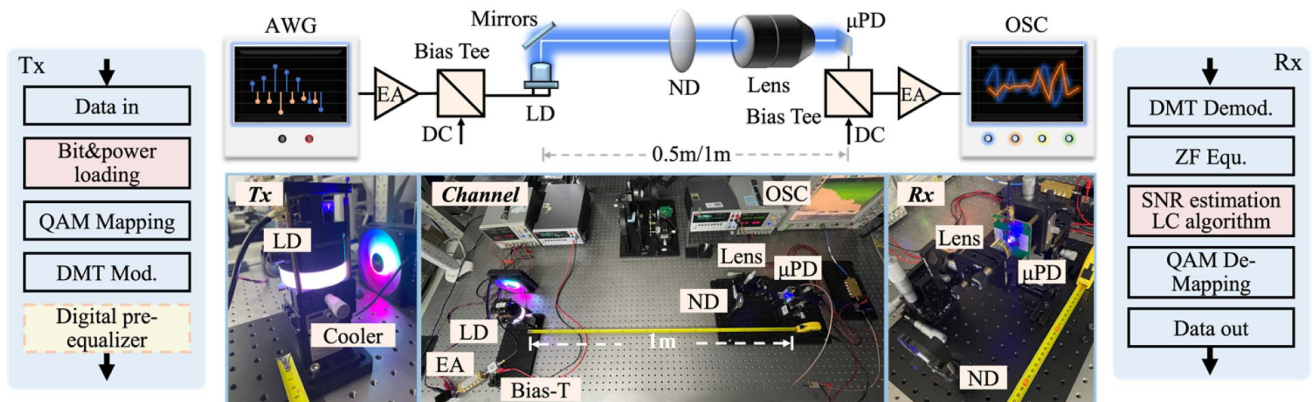


**Fig. 6.** Experimental setup of VLC system utilizing micro-LED-based photodetector.

$$x'(t) = \mathbb{F}^{-1}\{\mathbb{F}[x(t)] \cdot H_{\text{pre}}\}, \quad (2)$$

where  $x'(t)$  is the final transmitted signal.  $\mathbb{F}$  and  $\mathbb{F}^{-1}$  denote the FFT and IFFT.  $H_{\text{pre}}$  is the digital sampling of the hardware circuit frequency response  $H_{\text{eq}}$  in Ref. [49], expressed as

$$H_{\text{pre}}(\omega) = \sum_{k=0}^{N-1} H_{\text{eq}}(k\omega_s) \delta(\omega - k\omega_s), \quad (3)$$

where  $\delta$  is the frequency domain impulse function,  $\omega_s$  is the sampling angular frequency, and  $N$  is the signal data length.

Here, we redefine the hardware parameters by frequency domain equalized bandwidth  $f_0$ , maximum gain  $A_1$ , and gain  $A_2$  at  $f_0/2$ . The hardware parameters can be expressed as

$$R_4 = \frac{R_L}{10^{\frac{A_1}{10}} - 1}, \quad (4)$$

$$L_1 = \sqrt{\frac{(R_4 + R_L)^2 - 10^{\frac{A_2}{10}} R_4^2}{(10^{\frac{A_2}{10}} - 1) \left(\frac{4\pi f_0}{3}\right)^2}}, \quad (5)$$

$$C_1 = \frac{1}{L_1 (2\pi f_0)^2}. \quad (6)$$

Here,  $R_L$  is the resistance of load, and  $R_4$ ,  $L_1$ , and  $C_1$  are the resistance, inductance, and capacitance, respectively, which are all key parameters in Eq. (1) of [49].

At the receiver side, standard DMT demodulation is implemented. The channel recovery algorithm is a zero-forcing algorithm based on the training sequence. During the SNR estimation phase, the SNR for each subcarrier is determined by the constellation point-based error vector magnitude (EVM) [50]. At the bit power loading phase, the bit error rate (BER) is calculated after QAM de-mapping.

In the whole experiment, the SNR table used corresponds to the HD-FEC threshold of  $3.8 \times 10^{-3}$ . Therefore, the transmission rate  $R$  with 7% FEC overhead is calculated by the following equation:

$$R = \frac{R_{\text{Sampling}}}{2 \cdot u} \cdot \frac{N_{\text{sub}} - N_{\text{zero}}}{N_{\text{sub}}} \cdot M_{\text{SE}}, \quad (7)$$

where  $R_{\text{Sampling}}$  is the sampling rate of the arbitrary waveform generator (AWG).  $N_{\text{sub}}$  is the signal subcarrier number equal to 512.  $N_{\text{zero}}$  is the zero-padding subcarrier number equal to eight.  $M_{\text{SE}}$  is the average of the number of bits loaded in the valid subcarriers.

## B. Experimental Setup

Figure 6 shows the experimental setup of a 1 m VLC system utilizing a micro-LED-based PD. The transmitted DMT signal is generated by an offline MATLAB program and an AWG (Agilent M8190A). During the whole experiment, the sampling rate of AWG is set from 4.8 to 8.2 GSa/s. A 2.5 GHz EA (Mini-Circuits ZFL-2500VH+) and a 4.2 GHz bias tee (Mini-Circuits ZFBT-4R2GW-FT+) are employed to amplify the signal and drive the 450 nm LD (OSRAM PL450B). The LD is mounted on a compact optical platform and can be configured to form a tricolor LD [12]. In the entire experiment, we transmitted 0.5 and 1 m of free space.

At the receiver side, an adjustable neutral density (ND, Daheng Optics GCO-0702M) filter is used to control the light power incident into the PD. A lens (Olympus PLN10X/0.25) is utilized to facilitate the coupling of the optical signal into the micro-LED. The micro-LED-based PD is driven with reverse bias voltage provided by a constant-current source (Keithley 2400) and a 4.2 GHz bias tee. The output signal is again amplified by a 2.5 GHz EA and then sampled by the oscilloscope (OSC, Agilent MSO9254A). The sampling rate of the OSC is set at 5 GSa/s.

The entire DSP section is a standard bit-power loading DMT based on the LC algorithm, except for the use of a digital pre-equalizer. The specific processes can be found in the previous subsection. It is worth mentioning that the digital pre-equalizer process involves the optimization of specific parameters since it simulates a hardware pre-equalization circuit. For example, at a baudrate of 1.8 Gbaud,  $f_0$  is equal to 1.71 GHz,  $A_1$  is equal to 12 dB, and  $A_2$  is equal to 0.14 dB in this experiment.

## 4. EXPERIMENTAL RESULTS AND DISCUSSION

### A. System Optoelectronic Performance

First, we investigate the system's optoelectronic performance based on the setup in Fig. 6. The transmission distance is 0.5 m to simplify alignment and avoid channel effects on measurement performance. The frequency responses of the system with three micro-LEDs are measured using a network analyzer (Agilent N5230C), as shown in Figs. 7(a)–7(c). As can be seen from the results, the absolute values of the responses of all three sizes of micro-LEDs increase as the reverse bias voltage rises. At the same time, the bandwidth is also increasing with the voltage. The –3 dB cutoff bandwidths are 89.0, 88.8, and 43.0 MHz at –20 V. Since these values are slightly larger than the RC-delay bandwidth, the bandwidth of our device is limited mainly by the RC delay. This also means that optimizing the packaging process is expected to further increase the bandwidth. For example, chips can be connected in series to reduce capacitance. To better compare the bandwidth variation, Fig. 7(d) shows the –10 and –20 dB bandwidth changes with

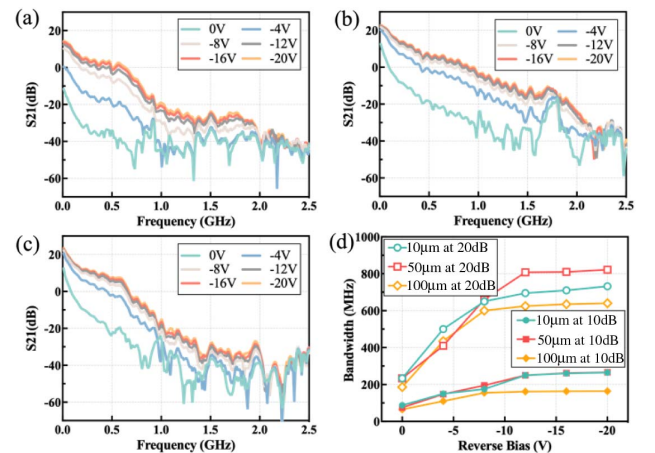


**Fig. 7.** Measured forward transmission gains of (a) 10 μm, (b) 50 μm, and (c) 100 μm micro-LED-based photodetectors; (d) 10 and 20 dB bandwidths versus reverse bias.



reverse bias voltages for three  $\mu$ PDs. As the voltage goes from 0 to  $-12$  V, the bandwidths of all three  $\mu$ PDs keep increasing. When  $-12$  V is exceeded, the bandwidth improvement gradually saturates. The trend of this change is related not only to the enhancement of the electric field and the increase in photocurrent, but also to the change of capacitance. The  $-20$  dB bandwidth of the  $10\ \mu\text{m}$   $\mu$ PD can be raised from 234 to 732 MHz as the voltage increases from 0 to  $-20$  V, while it is (234, 822) for  $50\ \mu\text{m}$  and (186, 640) for  $100\ \mu\text{m}$ . The  $\mu$ PD of  $100\ \mu\text{m}$  is minimum for either  $-10$  or  $-20$  dB bandwidth. This is because a larger photosensitive surface results in smaller light absorption per unit area and a smaller photogenerated carrier production rate when the incident power of light is constant [51]. But for  $10$  and  $50\ \mu\text{m}$   $\mu$ PDs, the  $-10$  dB bandwidth is almost the same;  $50\ \mu\text{m}$  has a larger  $-20$  dB bandwidth, which corresponds to a better high-frequency response. This is mainly because the  $10\ \mu\text{m}$  photosensitive surface is so small that the received light spot cannot be reduced to such a small size. This leads to a waste of part of the light signal. In addition to this,  $10\ \mu\text{m}$  has a higher dark current than  $50\ \mu\text{m}$ . This also leads to an increase in noise, which is more pronounced in the low-SNR region, such as the high-frequency region.

To further explore the SNRs of the three  $\mu$ PDs, the SNR performance is measured at 1 GHz bandwidth DMT signal. The results are presented in the form of box plots in Fig. 8. It shows the maximum, minimum, median, upper quartile, and lower quartile of the SNRs of the subcarriers at different voltages. As the reverse bias voltage increases, the maximum, minimum, and median SNRs increase for all three  $\mu$ PDs. The maximum-minimum SNR difference for both  $10$  and

$100\ \mu\text{m}$  is greater than for  $50\ \mu\text{m}$ , which is due to the fact that there has been some degradation in the high-frequency response at 1 GHz bandwidth for these two  $\mu$ PDs. Comparing the box size of the upper and lower quadrants, we can find that the communication performance of the  $10\ \mu\text{m}$   $\mu$ PD should be better than the  $100\ \mu\text{m}$  one, but much worse than the  $50\ \mu\text{m}$   $\mu$ PD.

## B. Performance of High-Speed Communication System

In this section, we investigate the transmission performances of  $\mu$ PDs. Figure 9 shows the variation of data rate with the peak-to-peak voltage ( $V_{pp}$ ) and the bias current of an LD at 0.5 m transmission distance. The sampling rates for  $10$ ,  $50$ , and  $100\ \mu\text{m}$  are set at 5.2, 7.6, and 5.2 GSa/s, respectively. The reverse bias voltages of all  $\mu$ PDs operate at  $-20$  V. The operation range is circled by a black line of 7.1 Gbps for  $10$  and  $100\ \mu\text{m}$ , and 10.6 Gbps for  $50\ \mu\text{m}$ . From the results, it is obvious that  $50\ \mu\text{m}$  has a better transmission rate. Comparing the operating range of  $10$  and  $100\ \mu\text{m}$ , it can be found that the  $10\ \mu\text{m}$   $\mu$ PD has a greater dynamic range compared to the  $100\ \mu\text{m}$ . This result is also consistent with the results of the SNR in Fig. 8. According to the measurement results, the optimal transmission points of  $10$ ,  $50$ , and  $100\ \mu\text{m}$   $\mu$ PD-based VLC systems are 0.7 V  $V_{pp}$  and 160 mA current, 1.0 V  $V_{pp}$  and 170 mA current, and 0.7 V  $V_{pp}$  and 170 mA current, respectively.

Figure 10(a) shows the data rate versus reverse bias voltage for  $10$ ,  $50$ , and  $100\ \mu\text{m}$   $\mu$ PDs. The results demonstrate that as the bias voltage rises, the transmission rate rises sharply

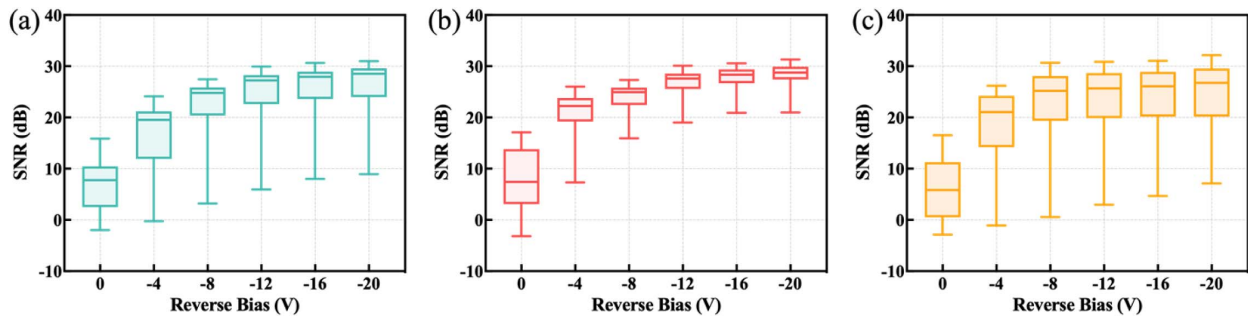


Fig. 8. SNR versus reverse bias for (a)  $10\ \mu\text{m}$ , (b)  $50\ \mu\text{m}$ , and (c)  $100\ \mu\text{m}$  micro-LED-based photodetectors.

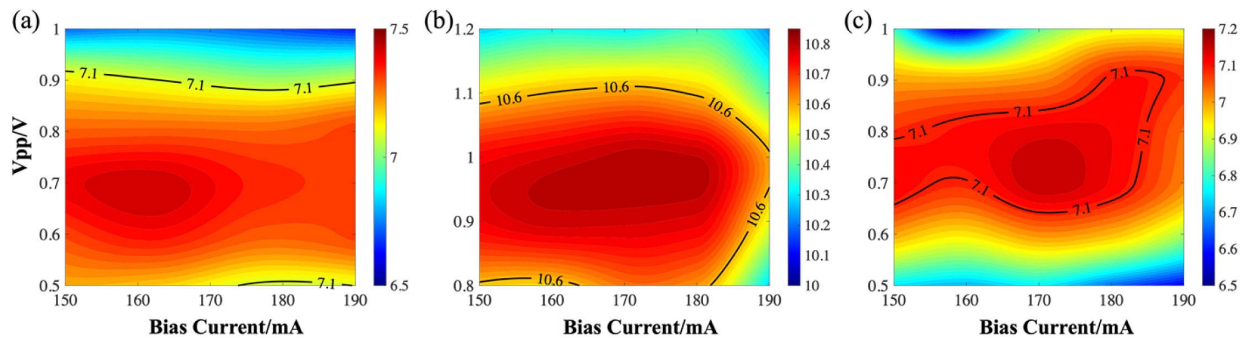
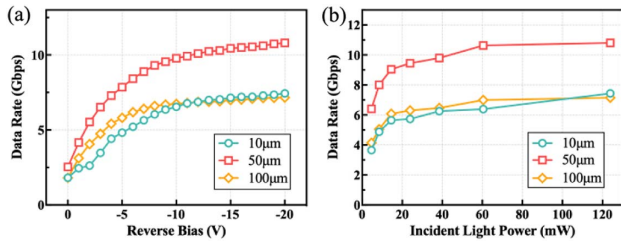


Fig. 9. Data rate versus bias current and signal  $V_{pp}$  for (a)  $10\ \mu\text{m}$ , (b)  $50\ \mu\text{m}$ , and (c)  $100\ \mu\text{m}$  micro-LED-based photodetectors.



**Fig. 10.** (a) Data rate versus reverse bias; (b) data rate versus incident light power for 10, 50, and 100  $\mu\text{m}$  micro-LED-based photodetectors.

and then tends to level off. Although GaN, as a wideband semiconductor, can support higher reverse bias voltages to obtain detection gain, in this experiment, the reverse bias voltage is only up to  $-20$  V to prevent reverse breakdown. According to the figures, all three  $\mu\text{PDs}$  start to enter the saturation zone at around  $-12$  V.

To analyze the reception performance of  $\mu\text{PDs}$ , we measure the relationship between incident light power and transmission data rates. The incident light power is controlled by the adjustable ND placed in front of the lens. The optical density (OD) parameter of the ND is 0–1.5, which means that the optical power can be attenuated to a minimum of 3% of the initial optical power. An integrating sphere photodiode power sensor (Thorlabs S142C) is utilized to measure the attenuated optical power. The results are shown in Fig. 10(b). According to the measured results, the optimal incident optical power for both 50 and 100  $\mu\text{m}$   $\mu\text{PDs}$  requires only about 60 mW, and higher optical power cannot improve the transmission rate. For the 10  $\mu\text{m}$   $\mu\text{PD}$ , the transmission rate still increases as the incident optical power increases. This is because even though the lens used is already an objective lens, the converged spot may still be larger than 10  $\mu\text{m}$ , resulting in not all of the incident optical power being received by the  $\mu\text{PD}$ . This also illustrates that

smaller  $\mu\text{PD}$  sizes make alignment more difficult. When the incident light power is minimized to 4.68 mW, the rates of 10, 50, and 100  $\mu\text{m}$   $\mu\text{PDs}$  are 3.65, 6.41, and 4.15 Gbps, respectively.

We further investigated the relationship between bandwidth and data rate. To transmit high-speed signals, a digital pre-equalizer is employed to simulate a hardware pre-equalization circuit. Figures 11(a)–11(c) show the electrical spectra of the original signal (without the digital pre-equalizer), transmitted signal, and received signal. The sampling rates for 10, 50, and 100  $\mu\text{m}$  are set at 4.8, 7.6, and 4.8 GSa/s, respectively. The baudrates are 1.2, 1.9, and 1.2 Gbaud, respectively. Considering zero padding, the effective signal bandwidths are 0.021–1.2, 0.033–1.9, and 0.021–1.2 GHz, respectively. As can be seen from the transmitted signal spectrum, the digital pre-equalizer slightly reduces the low-frequency component signal, with a 12 dB reduction in the lowest-frequency component. Even so, the spectrum of the received signal still shows that the low frequency is higher than the high frequency. The result of such a pre-compensation is also taken into account, in that overcompensation can lead to degradation of system performance [52]. Both the 10 and 100  $\mu\text{m}$  spectra start to drop off quickly and rapidly around 700 MHz, which is roughly near the  $-20$  dB bandwidth.

Figures 11(d)–11(f) illustrate the relationship between baudrate and data rate. The baudrate ranges from 1.2 to 1.6 Gbaud for 10 and 100  $\mu\text{m}$   $\mu\text{PDs}$ , and from 1.7 to 2.1 Gbaud for the 50  $\mu\text{m}$   $\mu\text{PD}$ . As the modulation bandwidth increases, the rate gradually reaches its highest point and then starts to decrease. The maximum data rate for the 10  $\mu\text{m}$   $\mu\text{PD}$  is 7.58 Gbps with 1.5 Gbaud, while it is 10.81 Gbps with 1.9 Gbaud for the 50  $\mu\text{m}$   $\mu\text{PD}$  and 7.18 Gbps with 1.4 Gbaud for the 100  $\mu\text{m}$   $\mu\text{PD}$ . The BER for each transmission data rate is under the HD-FEC threshold of  $3.8 \times 10^{-3}$ .

Finally, to show the effect of distance on data rate and to facilitate comparison with related work, a 1 m free space

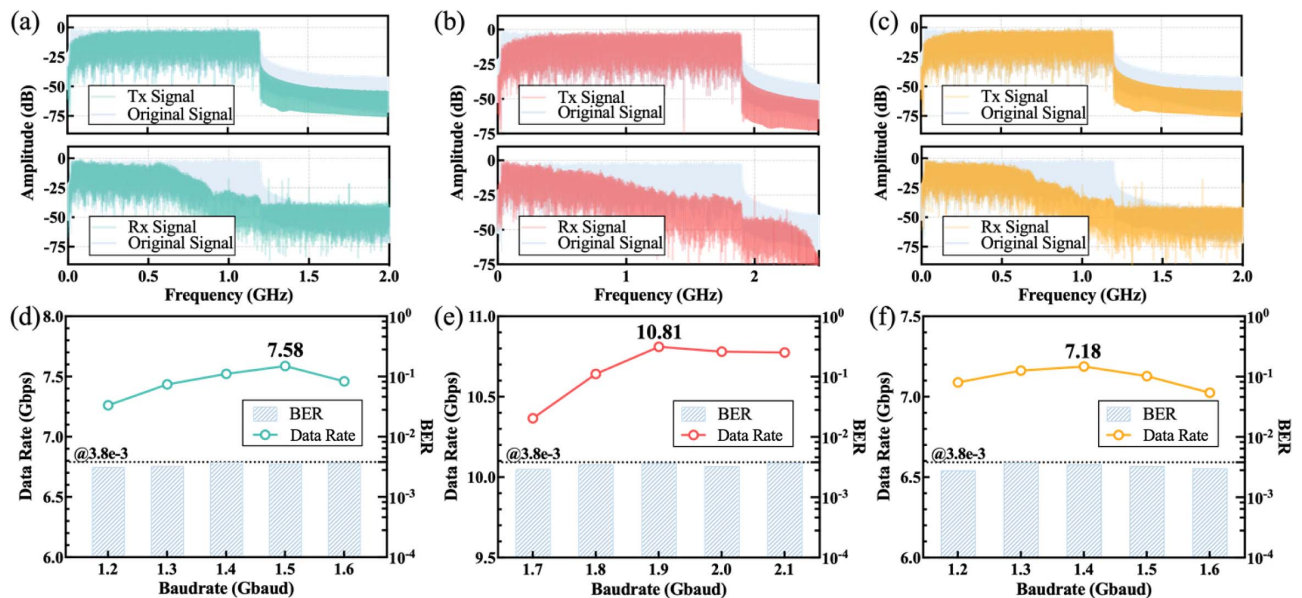


**Fig. 11.** Measured electrical spectra for (a) 10  $\mu\text{m}$ , (b) 50  $\mu\text{m}$ , and (c) 100  $\mu\text{m}$  micro-LED-based photodetectors; maximum data rate and BER versus baudrate at 0.5 m for (d) 10  $\mu\text{m}$ , (e) 50  $\mu\text{m}$ , and (f) 100  $\mu\text{m}$  micro-LED-based photodetectors.



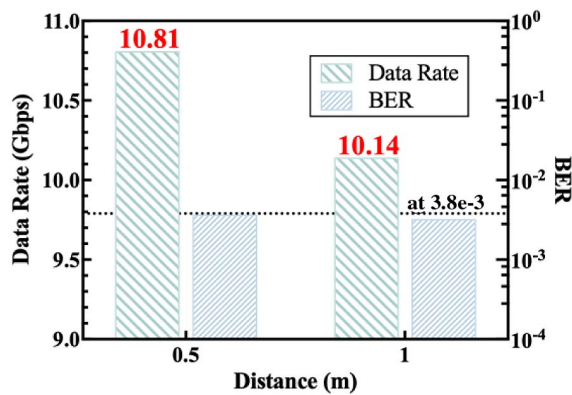


**Fig. 12.** Data rate and BER versus transmission distance for 50  $\mu\text{m}$  micro-LED-based photodetector.

VLC transmission experiment is demonstrated using the 50  $\mu\text{m}$   $\mu\text{PD}$  at 1.9 Gbaud. Figure 12 shows the performance results. As the transmission distance increases from 0.5 to 1 m, the transmission rate decreases only slightly, from 10.81 to 10.14 Gbps. The calculated BERs are  $3.677 \times 10^{-3}$  and  $3.244 \times 10^{-3}$ , respectively.

The detailed bit and power allocations of 0.5 and 1 m are shown in Fig. 13. In Fig. 13(a), the achievable average SE is  $5.7798 \text{ bit s}^{-1} \text{ Hz}^{-1}$ , while the mean SNR of subcarriers is 21.01 dB. Due to the digital pre-equalizer, the SNR is relatively low in the low-frequency region, with the highest SNR

occurring around 200 to 970 MHz. Among all subcarriers, the highest bit loading is  $8 \text{ bit s}^{-1} \text{ Hz}^{-1}$ , and the lowest bit loading is  $2 \text{ bit s}^{-1} \text{ Hz}^{-1}$ . The constellations of 256-QAM, 128-QAM, 64-QAM, 32-QAM, 16-QAM, 8-QAM, and QPSK are also shown in the insets of Fig. 13(a). For 1 m transmission distance, the SE is  $5.4226 \text{ bit s}^{-1} \text{ Hz}^{-1}$  and the SNR is 19.90 dB, as shown in Fig. 13(b). Due to the increase in transmission distance, there is a slight deterioration in performance, with the highest SNR occurring at only around 225–810 MHz. Meanwhile, there is one subcarrier that can support only binary phase-shift keying (BPSK) modulation. The QAM constellation diagrams are also shown in the insets of Fig. 13(b). There is no BPSK constellation diagram because there are too few BPSK subcarriers. Figures 13(c) and 13(d) show power allocations of 0.5 and 1 m transmission distance. The power ratios fluctuate between 0.72 and 1.19, and the minimum values occur in the high-frequency part.

To compare the results of recent micro-LED-based PDs, we have summarized the relevant results, as shown in Table 2. Neither the sapphire-substrate nor the GaN-substrate  $\mu\text{PDs}$  have achieved transmission rates above 10 Gbps. This is probably due to the low thermal conductivity of the sapphire substrate when high incident light power is present, which results in current crowding and current droop. GaN substrates, on the other hand, have the potential for high speed, but may require better chip design. In addition, the SE of OOK modulation is too low compared to OFDM modulation to achieve high-speed transmission. Compared with the results for a transmission

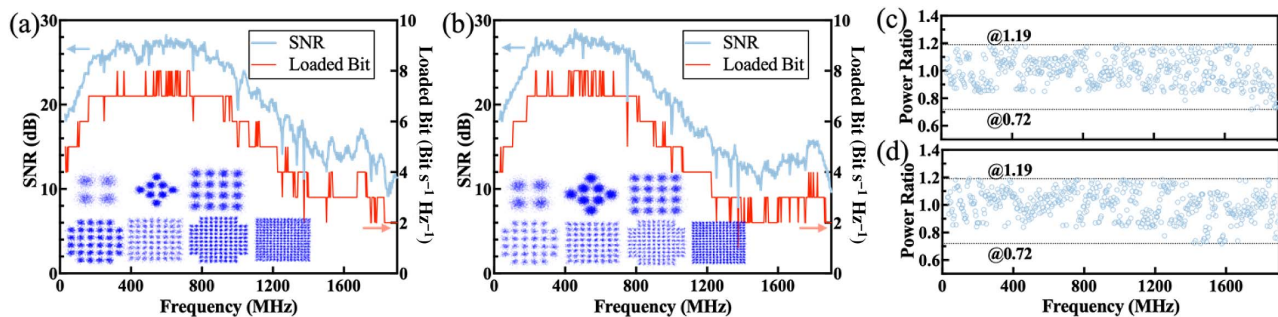


**Fig. 13.** SNR and bit number versus frequency at 1.9 Gbaud for (a) 0.5 m and (b) 1 m transmission distance; power ratio versus frequency for (c) 0.5 m and (d) 1 m.

**Table 2.** Recent Achievements of Micro-LED-Based Photodetectors

Year	Substrate	Array	Bias	Peak Response		Modulation Format	Data Rate (Gbps)	Distance	Reference
				Wavelength	FWHM				
2018	Sapphire	—	−3 V	392 nm	34 nm	OFDM	3.2	0.5 m fiber and 0.1 m free space	[17]
2019	Sapphire	Not mentioned	−5 V	405 nm	—	OOK	0.35	1 m free space	[26]
2019	GaN	—	−10 V	400 nm	40 nm	OOK	1.55	1 m free space	[27]
2020	GaN	—	−8 V	400 nm	60 nm	BPL-OFDM	7.4	1 m free space	[28]
2021	Sapphire	Not mentioned	−5 V	—	—	OOK	0.06	2.3 m underwater	[29]
2021	Sapphire	2 × 4	−5 V	—	—	OOK	0.3	1.25 m free space	[30]
2021	Sapphire	2 × 4	−5 V	—	—	OOK	0.54	1.1 m free space	[31]
2022	Si	4 × 4	−20 V	425 nm	—	BPL-OFDM	8.205	0.5 m free space	[36]
2022	Si	4 × 4	−20 V	400 nm	72 nm	BPL-DMT	10.14	1 m free space	This work

distance of 1 m and transmission rate of 7.4 Gbps [28], the present work increases the data rate by approximately 3 Gbps for the same transmission distance, using the similar bit power loading multicarrier modulation method. The 72 nm FWHM significantly enhances the feasibility of  $\mu$ PDs in VLC systems. To the best of our knowledge, this is the highest transmission rate for InGaN/GaN micro-LED-based PDs, and the first time that a data rate of 10 Gbps has been reached. Furthermore, it is anticipated that such a high-speed  $\mu$ PD will also be accessible as a high-speed transmitter, which has the potential to allow the design of transmitter chips and receiver chips to learn from each other.

## 5. CONCLUSION

In this paper, an InGaN/GaN MQW-based vertical-structure  $\mu$ PD on a Si substrate is proposed as a receiver to achieve a 10 Gbps VLC system with a 450 nm LD. The photoelectrical performances of our constructed  $\mu$ PDs of three various sizes, 10, 50, and 100  $\mu$ m, are investigated. At low current density, the emission peak wavelengths are 626, 596, and 600 nm for 10, 50, and 100  $\mu$ m micro-LEDs, respectively. As a receiver, the peak responsivity of all three  $\mu$ PDs is achieved at 400 nm, while the passband FWHMs are 87 nm (375–462 nm), 72 nm (382–454 nm), and 78 nm (382–460 nm) for 10, 50, and 100  $\mu$ m  $\mu$ PDs. Unfortunately, the bandwidth of our device is limited mainly by the RC delay, although this can be addressed in the future via package optimization and better chip fabrication. Utilizing the self-designed  $4 \times 4$  50  $\mu$ m  $\mu$ PD array, a 10.14 Gbps 1 m VLC link is experimentally demonstrated by bit and power loading DMT modulation and the proposed digital pre-equalizer algorithm under the HD-FEC threshold of  $3.8 \times 10^{-3}$ . This is the first time a transmission rate of more than 10 Gbps has been achieved using a GaN-based PD, to the best of our knowledge. These findings reveal that Si substrates and vertical architectures are superior in InGaN/GaN  $\mu$ PDs, and that they have a lot of potential for high-speed VLC links beyond 10 Gbps.

**Funding.** National Natural Science Foundation of China (61925104, 62031011, 62201157); Major Key Project of PCL; China Postdoctoral Science Foundation (2021M700025); National Postdoctoral Program for Innovative Talents (BX2021082).

**Disclosures.** The authors declare no conflicts of interest.

**Data Availability.** Data underlying the results presented in this paper are not publicly available at this time but may be obtained from the authors upon reasonable request.

## REFERENCES

- X. You, C.-X. Wang, J. Huang, X. Gao, Z. Zhang, M. Wang, Y. Huang, C. Zhang, Y. Jiang, and J. Wang, "Towards 6G wireless communication networks: vision, enabling technologies, and new paradigm shifts," *Sci. China Inf. Sci.* **64**, 110301 (2021).
- M. Latva-aho, K. Leppänen, F. Clazzer, and A. Munari, *Key Drivers and Research Challenges for 6G Ubiquitous Wireless Intelligence* (Jultika, 2019).
- N. Chi, H. Haas, M. Kavehrad, T. D. Little, and X.-L. Huang, "Visible light communications: demand factors, benefits and opportunities [Guest Editorial]," *IEEE Wireless Commun.* **22**, 5–7 (2015).
- N. Chi, Y. Zhou, Y. Wei, and F. Hu, "Visible light communication in 6G: advances, challenges, and prospects," *IEEE Veh. Technol. Mag.* **15**, 93–102 (2020).
- B. Zong, C. Fan, X. Wang, X. Duan, B. Wang, and J. Wang, "6G technologies: key drivers, core requirements, system architectures, and enabling technologies," *IEEE Veh. Technol. Mag.* **14**, 18–27 (2019).
- R. Bian, I. Tavakkolnia, and H. Haas, "15.73 Gb/s visible light communication with off-the-shelf LEDs," *J. Lightwave Technol.* **37**, 2418–2424 (2019).
- E. Xie, R. Bian, X. He, M. S. Islim, C. Chen, J. J. McKendry, E. Gu, H. Haas, and M. D. Dawson, "Over 10 Gbps VLC for long-distance applications using a GaN-based series-biased micro-LED array," *IEEE Photon. Technol. Lett.* **32**, 499–502 (2020).
- F. Hu, S. Chen, G. Li, P. Zou, J. Zhang, J. Hu, J. Zhang, Z. He, S. Yu, and F. Jiang, "Si-substrate LEDs with multiple superlattice interlayers for beyond 24 Gbps visible light communication," *Photon. Res.* **9**, 1581–1591 (2021).
- D. Li, C. Ma, J. Wang, F. Hu, Y. Hou, S. Wang, J. Hu, S. Yi, Y. Ma, and J. Shi, "High-speed GaN-based superluminescent diode for 4.57 Gbps visible light communication," *Crystals* **12**, 191 (2022).
- C. Shen, C. Lee, T. K. Ng, S. Nakamura, J. S. Speck, S. P. DenBaars, A. Y. Alyamani, M. M. El-Desouki, and B. S. Ooi, "High-speed 405-nm superluminescent diode (SLD) with 807-MHz modulation bandwidth," *Opt. Express* **24**, 20281–20286 (2016).
- F. Hu, J. A. Holguin-Lerma, Y. Mao, P. Zou, C. Shen, T. K. Ng, B. S. Ooi, and N. Chi, "Demonstration of a low-complexity memory-polynomial-aided neural network equalizer for CAP visible-light communication with superluminescent diode," *Opto-Electron. Adv.* **3**, 200009 (2020).
- J. Hu, F. Hu, J. Jia, G. Li, J. Shi, J. Zhang, Z. Li, N. Chi, S. Yu, and C. Shen, "46.4 Gbps visible light communication system utilizing a compact tricolor laser transmitter," *Opt. Express* **30**, 4365–4373 (2022).
- W.-C. Wang, C.-H. Cheng, H.-Y. Wang, and G.-R. Lin, "White-light color conversion with red/green/violet laser diodes and yellow light-emitting diode mixing for 34.8 Gbit/s visible lighting communication," *Photon. Res.* **8**, 1398–1408 (2020).
- J. Lavrencik, S. Varughese, V. A. Thomas, G. Landry, Y. Sun, R. Shubochkin, K. Balemarthy, J. Tatum, and S. E. Ralph, " $4\lambda \times 100$  Gbps VCSEL PAM-4 transmission over 105 m of wide band multimode fiber," in *Optical Fiber Communication Conference* (Optical Society of America, 2017), paper Tu2B.6.
- T.-C. Wu, Y.-C. Chi, H.-Y. Wang, C.-T. Tsai, and G.-R. Lin, "Blue laser diode enables underwater communication at 12.4 Gbps," *Sci. Rep.* **7**, 1 (2017).
- X. Liu, S. Yi, X. Zhou, Z. Fang, Z.-J. Qiu, L. Hu, C. Cong, L. Zheng, R. Liu, and P. Tian, "34.5 m underwater optical wireless communication with 2.70 Gbps data rate based on a green laser diode with NRZ-OOK modulation," *Opt. Express* **25**, 27937–27947 (2017).
- K.-T. Ho, R. Chen, G. Liu, C. Shen, J. Holguin-Lerma, A. A. Al-Saggaf, T. K. Ng, M.-S. Alouini, J.-H. He, and B. S. Ooi, "3.2 Gigabit-per-second visible light communication link with InGaN/GaN MQW micro-photodetector," *Opt. Express* **26**, 3037–3045 (2018).
- D. Walker, E. Monroy, P. Kung, J. Wu, M. Hamilton, F. Sanchez, J. Diaz, and M. Razeghi, "High-speed, low-noise metal-semiconductor-metal ultraviolet photodetectors based on GaN," *Appl. Phys. Lett.* **74**, 762–764 (1999).
- Y.-K. Su, Y.-Z. Chiou, F.-S. Juang, S.-J. Chang, and J.-K. Sheu, "GaN and InGaN metal-semiconductor-metal photodetectors with different Schottky contact metals," *Jpn. J. Appl. Phys.* **40**, 2996–2999 (2001).
- J. Carrano, T. Li, D. Brown, P. Grudowski, C. Eiting, R. Dupuis, and J. Campbell, "Very high-speed metal-semiconductor-metal ultraviolet photodetectors fabricated on GaN," *Appl. Phys. Lett.* **73**, 2405–2407 (1998).
- B. Butun, T. Tut, E. Ulker, T. Yelboga, and E. Ozbay, "High-performance visible-blind GaN-based p-i-n photodetectors," *Appl. Phys. Lett.* **92**, 033507 (2008).

22. G. Xu, A. Salvador, W. Kim, Z. Fan, C. Lu, H. Tang, H. Morkoç, G. Smith, M. Estes, and B. Goldenberg, "High speed, low noise ultraviolet photodetectors based on GaN pin and AlGaIn (p)-GaIn (i)-GaIn (n) structures," *Appl. Phys. Lett.* **71**, 2154–2156 (1997).
23. E. Miyazaki, S. Itami, and T. Araki, "Using a light-emitting diode as a high-speed, wavelength selective photodetector," *Rev. Sci. Instrum.* **69**, 3751–3754 (1998).
24. B. Alshehri, K. Dogheche, S. Belahsene, A. Ramdane, G. Patriarche, D. Decoster, and E. Dogheche, "Dynamic characterization of III-nitride-based high-speed photodiodes," *IEEE Photon. J.* **9**, 6803107 (2017).
25. C. Shen, C. Lee, E. Stegenburgs, J. H. Lerma, T. K. Ng, S. Nakamura, S. P. DenBaars, A. Y. Alyamani, M. M. El-Desouki, and B. S. Ooi, "Semipolar III-nitride quantum well waveguide photodetector integrated with laser diode for on-chip photonic system," *Appl. Phys. Express* **10**, 042201 (2017).
26. X. Liu, R. Lin, H. Chen, S. Zhang, Z. Qian, G. Zhou, X. Chen, X. Zhou, L. Zheng, and R. Liu, "High-bandwidth InGaIn self-powered detector arrays toward MIMO visible light communication based on micro-LED arrays," *ACS Photon.* **6**, 3186–3195 (2019).
27. C. H. Kang, G. Liu, C. Lee, O. Alkhazragi, J. M. Wagstaff, K.-H. Li, F. Alhawaj, T. K. Ng, J. S. Speck, and S. Nakamura, "Semipolar (20 $\bar{2}$ 1) InGaIn/GaN micro-photodetector for gigabit-per-second visible light communication," *Appl. Phys. Express* **13**, 014001 (2019).
28. O. Alkhazragi, C. H. Kang, M. Kong, G. Liu, C. Lee, K.-H. Li, H. Zhang, J. M. Wagstaff, F. Alhawaj, and T. K. Ng, "7.4-Gbit/s visible-light communication utilizing wavelength-selective semipolar micro-photodetector," *IEEE Photon. Technol. Lett.* **32**, 767–770 (2020).
29. R. Lin, X. Liu, G. Zhou, Z. Qian, X. Cui, and P. Tian, "InGaIn Micro-LED array enabled advanced underwater wireless optical communication and underwater charging," *Adv. Opt. Mater.* **9**, 2002211 (2021).
30. Y.-H. Chang, F.-J. Liou, W. H. Gunawan, C.-W. Chow, Y. Liu, H.-C. Kuo, and C.-H. Yeh, "High bandwidth semipolar (20-21)  $\mu$ -LED serving as photo-receiver for visible light communication," in *European Conference on Optical Communication (ECOC)* (IEEE, 2021), pp. 1–4.
31. Y.-H. Chang, T.-C. Hsu, F.-J. Liou, C.-W. Chow, Y. Liu, H.-C. Kuo, C.-H. Yeh, and P.-H. Yang, "High-bandwidth InGaIn/GaN semipolar micro-LED acting as a fast photodetector for visible light communications," *Opt. Express* **29**, 37245–37252 (2021).
32. A. T. Hussein and J. M. Elmirghani, "10 Gbps mobile visible light communication system employing angle diversity, imaging receivers, and relay nodes," *J. Opt. Commun. Netw.* **7**, 718–735 (2015).
33. C. Xiong, F. Jiang, W. Fang, L. Wang, H. Liu, and C. Mo, "Different properties of GaIn-based LED grown on Si (111) and transferred onto new substrate," *Sci. China Ser. E* **49**, 313–321 (2006).
34. Y. Zhou, X. Zhu, F. Hu, J. Shi, F. Wang, P. Zou, J. Liu, F. Jiang, and N. Chi, "Common-anode LED on a Si substrate for beyond 15 Gbit/s underwater visible light communication," *Photon. Res.* **7**, 1019–1029 (2019).
35. K. Saron, M. Hashim, and M. Farrukh, "Growth of GaIn films on silicon (1 1 1) by thermal vapor deposition method: optical functions and MSM UV photodetector applications," *Superlattices Microstruct.* **64**, 88–97 (2013).
36. W. Niu, J. Shi, Z. Xu, D. Li, W. Xiao, G. Wang, J. Zhang, Z. He, C. Shen, and N. Chi, "8.205-Gbit/s visible light communication utilizing 4  $\times$  4 Si-substrate  $\mu$ LED-based photodetector array," in *Optical Fiber Communication Conference* (Optica Publishing Group, 2022), paper Tu3C.2.
37. A. Krost and A. Dadgar, "GaIn-based optoelectronics on silicon substrates," *Mater. Sci. Eng. B* **93**, 77–84 (2002).
38. F. Jiang, J. Liu, L. Wang, C. Xiong, W. Fang, C. Mo, Y. Tang, G. Wang, L. Xu, and J. Ding, "High optical efficiency GaIn based blue LED on silicon substrate," *Sci. Sin. Phys. Mech. Astron.* **45**, 067302 (2015).
39. Z. Quan, J. Liu, F. Fang, G. Wang, and F. Jiang, "Effect of V-shaped pit area ratio on quantum efficiency of blue InGaIn/GaN multiple-quantum well light-emitting diodes," *Opt. Quantum Electron.* **48**, 195 (2016).
40. Z. Quan, L. Wang, C. Zheng, J. Liu, and F. Jiang, "Roles of V-shaped pits on the improvement of quantum efficiency in InGaIn/GaN multiple quantum well light-emitting diodes," *J. Appl. Phys.* **116**, 183107 (2014).
41. G. Wang, C. Xiong, J. Liu, and F. Jiang, "Improving p-type contact characteristics by Ni-assisted annealing and effects on surface morphologic evolution of InGaIn LED films grown on Si (1 1 1)," *Appl. Surf. Sci.* **257**, 8675–8678 (2011).
42. F. Jiang, L. Wang, and W. Fang, "Semiconductor light-emitting device and method for making same," U.S. patent 7,919,784 (April 5, 2011).
43. K. Wada, H. Yoshioka, J. Zhu, T. Matsuyama, and H. Horinaka, "Simple form of multimode laser diode rate equations incorporating the band filling effect," *Opt. Express* **19**, 3019–3036 (2011).
44. J. Campello, "Practical bit loading for DMT," in *IEEE International Conference on Communications* (IEEE, 1999), pp. 801–805.
45. J. Campello, "Optimal discrete bit loading for multicarrier modulation systems," in *IEEE International Symposium on Information Theory* (IEEE, 1998), p. 193.
46. X. Huang, J. Shi, J. Li, Y. Wang, and N. Chi, "A Gb/s VLC transmission using hardware preequalization circuit," *IEEE Photon. Technol. Lett.* **27**, 1915–1918 (2015).
47. X. Huang, S. Chen, Z. Wang, Y. Wang, and N. Chi, "1.2 Gbit/s visible light transmission based on orthogonal frequency-division multiplexing using a phosphorescent white light-emitting diode and a pre-equalization circuit," *Chin. Opt. Lett.* **13**, 100602 (2015).
48. X. Huang, Z. Wang, J. Shi, Y. Wang, and N. Chi, "1.6 Gbit/s phosphorescent white LED based VLC transmission using a cascaded pre-equalization circuit and a differential outputs PIN receiver," *Opt. Express* **23**, 22034–22042 (2015).
49. X. Huang, S. Chen, Z. Wang, J. Shi, Y. Wang, J. Xiao, and N. Chi, "2.0-Gb/s visible light link based on adaptive bit allocation OFDM of a single phosphorescent white LED," *IEEE Photon. J.* **7**, 7904008 (2015).
50. R. A. Shafik, M. S. Rahman, and A. R. Islam, "On the extended relationships among EVM, BER and SNR as performance metrics," in *International Conference on Electrical and Computer Engineering (ICECE)* (IEEE, 2006), pp. 408–411.
51. F. Xue, L. Yang, M. Chen, J. Chen, X. Yang, L. Wang, L. Chen, C. Pan, and Z. L. Wang, "Enhanced photoresponsivity of the MoS<sub>2</sub>-GaIn heterojunction diode via the piezo-phototronic effect," *NPG Asia Mater.* **9**, e418 (2017).
52. P. Zou, Y. Zhao, F. Hu, and N. Chi, "Underwater visible light communication at 3.24 Gb/s using novel two-dimensional bit allocation," *Opt. Express* **28**, 11319–11338 (2020).